Journal of Mechanics in Medicine and Biology
Vol. 18, No. 5 (2018) 1850055 (16 pages)

DOI: 10.1142/S0219519418500550

World Scientific
www.worldscientific.com

STUDY ON THE RELATIONSHIP BETWEEN WALL SHEAR STRESS AND ASPECT RATIO OF CEREBRAL ANEURYSMS WITH DIFFERENT PRESSURE DIFFERENCES USING CFD SIMULATIONS

ALFREDO ARANDA* and ALVARO VALENCIA
Department of Mechanical Engineering
Universidad de Chile, Beauchef 851, Santiago 8370456, Chile
**alfredo.arandan@gmail.com*

Received 2 March 2018
Revised 12 June 2018
Accepted 1 July 2018
Published 3 August 2018

CFD simulations were performed for 60 human cerebral aneurysms (30 previously ruptured and 30 previously unruptured) to study the behavior of the time-averaged wall shear stress (TAWSS) with respect to the aspect ratio (AR), implementing a set of low, normal, and high-pressure differences between the inlet and the outlets of each artery. It is well known that there exists a direct relationship between TAWSS and the rupture. In this investigation, we presented an important result because the condition of the pressure among the branches and the AR may be measured in any patient, then a slope may be associated, and finally a TAWSS may be estimated. We found that when the pressure difference increased, the absolute slopes between TAWSS and AR increased as well. Also, the magnitude of the slope in the previously unruptured aneurysms was 4.7 times the slope in the previously ruptured aneurysms. On the other hand, TAWSS was higher in the previously unruptured aneurysm than previously ruptured aneurysms due to the unruptured aneurysms that have a smaller surface area. Furthermore, we analyzed the relationship between TAWSS and other geometric parameters of the aneurysm, such as bottleneck and non-sphericity index; however, no correlation was found for either cases.

Keywords: CFD; cerebral aneurysm simulations; pressure difference; wall shear stress; aspect ratio.

1. Introduction

An intracranial aneurysm (also called brain or cerebral aneurysm) is an abnormal dilation of an artery caused by a weakness on the wall (a reduction in the tunica media, i.e., muscular middle layer of the artery wall due to certain hemodynamic factors[1]), and it is located in the subarachnoid space at the base of the brain.[2] It is

*Corresponding author.

typically classified based on its form and position in the main artery into the terminal, lateral, or bifurcation aneurysm.[3] High-blood pressure, smoking, family history, a previous aneurysm, and gender are factors that may increase the rupture risk of an aneurysm. A study of the unruptured cerebral aneurysms revealed that the rupture rate of a small aneurysm was only 0.05% per annum in patients with no prior incidence of subarachnoid hemorrhage, and 0.5% per annum for large aneurysms (> 10 mm diameter) in patients with previous incidence of subarachnoid hemorrhage.[4] Also, clinical studies have demonstrated that Wall Shear Stress (WSS) and velocity field inside the arteries are relevant to understand the formation of aneurysms and the ruptures.[5,6] On the other hand, a complete study of the aneurysm hemodynamic is possible via computational fluid dynamics (CFD) using reconstructed cerebral aneurysm models. In fact, three computational studies are known to have demonstrated that CFD may be used to differentiate between a ruptured and non-ruptured cerebral aneurysm.[7–9]

Hemodynamic stresses are considered as important factors affecting the development of aneurysms because they are directly related with aneurysm rupture.[5,6] One of the hemodynamic factors, WSS, acts directly on the vascular endothelium as a biological stimulator that modulates its cellular function.[10–12] Some authors have proposed a relationship between WSS, calculated from computational simulations, and the aspect ratio (AR) to determine the rupture risk.[13,14] Tateshima *et al.*[15] determined a linear relationship between WSS and AR with a negative slope. Ujie *et al.*[16] found an important result indicating that the difference between the ARs of ruptured and unruptured aneurysms was statistically significant, and therefore, it could become a reliable index for predicting an aneurysm rupture and help to accurately analyze the operative indications to perform surgeries on an incidentally discovered unruptured aneurysm. Shojima *et al.*[12] illustrated that a low WSS may facilitate the growth phase of a cerebral aneurysm and trigger its rupture by causing degenerative changes in the aneurysm wall. Consequently, the WSS on an aneurysm region related with respect to the AR may be of some assistance in the prediction of its rupture.

2. Methodology

2.1. *Reconstruction of geometries and properties*

The geometric dimensions of an aneurysm (height in yellow, neck diameter in green and width in cyan) are shown in Fig. 1(a). The AR (neck-to-dome length/neck-width) was calculated for the entire cerebral aneurysm geometries, wherein AR values from 0.6337 to 5.2786 were considered.

The models shown in Fig. 1(a) were generated by first performing aneurysm surgeries of the patients of Instituto de Neurocirugía Asenjo (INCA), and then, reconstructing 60 three-dimensional angiography images on a 1:1 scale to obtain an adequate geometry for the simulation software, ANSYS (shown in Fig. 1(b)). In this

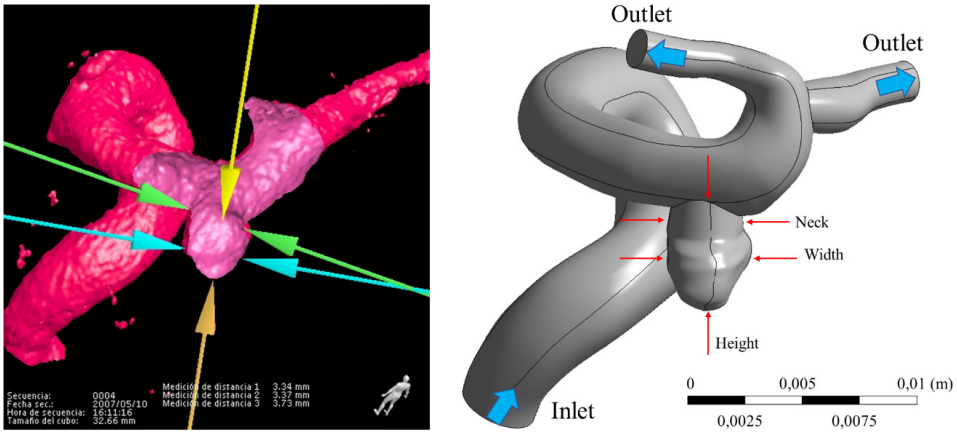

(a) (b)

Fig. 1. (a) Three-dimensional angiography image from a patient of INCA. (b) Reconstruction from the three-dimensional angiography with an inlet, outlets and the aneurysm geometric measurement (Neck, Width, and Height).

investigation, 30 aneurysms were previously ruptured and other 30 were previously unruptured.

To model the blood inside each artery, a laminar and incompressible fluid flow was considered using $\rho = 1065\,\mathrm{kg/m}^3$[17,18] and modeled by the conservation of mass and momentum (Navier–Stokes equations). Also, it was considered as a non-Newtonian fluid, and the Carreau model was used to model the shear thinning behavior[19]:

$$\mu_{\mathrm{eff}}(\dot{\gamma}) = \mu_{\mathrm{inf}} + (\mu_0 - \mu_{\mathrm{inf}})(1 + (\lambda\dot{\gamma})^2)^{\frac{n-1}{2}}, \tag{1}$$

where $\mu_{\mathrm{inf}} = 0.00345\,\mathrm{kg/m \cdot s}$ (viscosity at infinite shear rate), $\mu_0 = 0.056\,\mathrm{kg/m \cdot s}$ (viscosity at zero shear rate), $\lambda = 3.313\,\mathrm{s}$ (relaxation time), and $n = 0.3568$ (power index) are the material coefficients.

With respect to the mechanical behavior of the artery walls, we considered the simplification of the rigid artery in all cases.

2.2. *Boundary conditions*

It is important to mention that the boundary conditions simulated the internal cardiovascular system of the brain and these ones should be adjusted to maximize the real conditions, having an important role in the development of the flow inside each artery. The inlet condition was used as a velocity profile and the outlet conditions represented the blood pressure. The pressure difference was another important factor that was assumed to be only a function of time, and it was generated by a pulse wave of a finite velocity.[20] We used the Womersley velocity theory[21] to obtain the physiological flow conditions at the artery inlet. The velocity profile was

computed from the general Womersley solution (Eq. (2)) using a code on RStudio and it was subsequently exported to the ANSYS Fluent software[22] (the Womersley solution equation is described in more detail in Ref. 21).

$$v(r,t) = \frac{2Q_0}{\pi a^2}\left[1-\left(\frac{r}{a}\right)^2\right] + \sum_{n=1}^{N}\frac{Q_n}{\pi a^2}\left[\frac{1-\frac{J_0\left(\frac{\beta_n r}{a}\right)}{J_0(\beta_n)}}{1-\frac{2J_1(\beta_n)}{\beta_n J_0(\beta_n)}}\right]e^{in\omega t}, \tag{2}$$

with

$$\beta_n = i^{\frac{3}{2}}\alpha_n = i^{\frac{3}{2}}a\sqrt{\frac{n\omega}{\nu}}, \tag{3}$$

where α_n is the n-Womersley number, a is the artery radius of the inlet, n is the number of modes, and ω is the angular frequency obtained from the period of the cardiac cycle. In our study, we have chosen eight modes and an angular frequency of $7.703\,\mathrm{s}^{-1}$ (period of the cardiac cycle was 0.857 s). The Womersley solution depends on the Womersley number, and it is a measure of the ratio of the momentum equation to the viscous part.[23] When α_n is small, the unsteadiness is not important, and the solutions become Poiseuille solutions that vary in magnitude, but not in shape. If α_n is large, the shapes of the profiles are not parabolic.[21]

Figure 2(a) shows one of the 60 blood velocity profile measurements delivered by INCA. We obtained the time-averaged maximum velocity (TAMAX) following the results given by Li *et al.*[24] and Blanco[25] for all artery-images using an RStudio tool.[26] We localized each RGB pixel of the TAMAX line (a smooth line of Fig. 2(a)), then, we related the distance between a subtraction of pixels and a subtraction of centimeters at the vertical axis. Finally, an average was derived from all the velocity profiles and it was multiplied by the inlet area of each geometry to obtain the blood flow (Q_i), assuming that the vessels were circular in cross-section (shown in Fig. 2(b)). Subsequently, a Fourier fitting of Q_i was performed using a fit function of

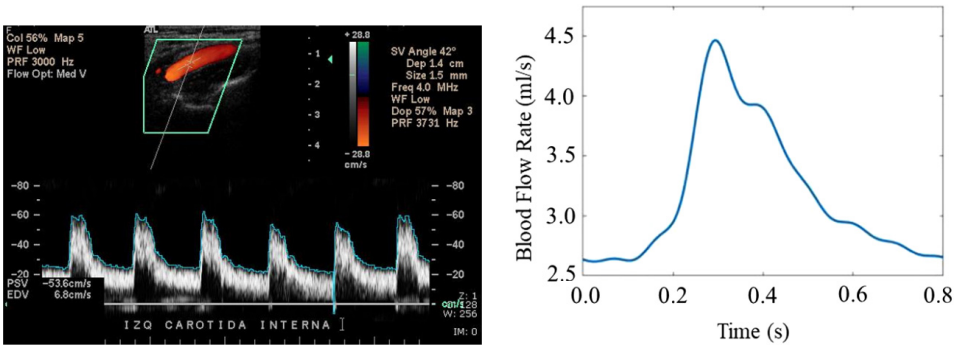

(a) (b)

Fig. 2. (a) Blood velocity measurement from a patient of INCA. (b) Flow volume to employ in the inlet condition.

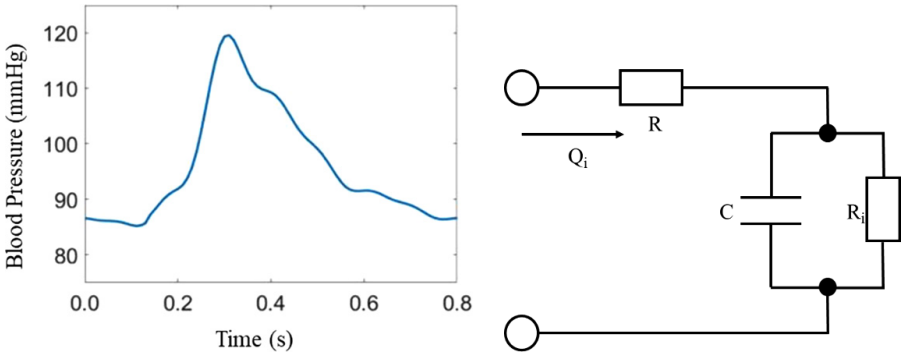

(a) (b)

Fig. 3. (a) Equivalent pulsatile pressure computed by the (b) three-element Windkessel model.

RStudio to obtain the respective Fourier coefficients.[27] Finally, the Fourier coefficients were employed to calculate the Womersley velocity of each geometry.

The maximum flow volume calculated was 270 ml/min, shown in the peak of Fig. 2(b). This result is in accordance with the results given by Leopold *et al.*,[28] Schoning *et al.*,[29] Scheel *et al.*,[30] and Kamensky.[31]

We used a normal pulsatile pressure condition between 80 mmHg and 120 mmHg[32] (shown in Fig. 3(a)) calculated through a three-element Windkessel model (Fig. 3(b)) for the outlets, using two resistors and a capacitance. The purpose of this model was to represent the realistic physiological flow patterns and pressure distributions in the computational domain for the fluid.[33]

The differential equation that describes the circuit of Fig. 3(b) (Eq. (4)) is

$$\frac{dp_i}{dt} + \frac{p_i}{RC} = \frac{Q_i}{C}\left(1 + \frac{R_i}{R}\right) + R_i \frac{dQ_i}{dt}, \tag{4}$$

where p_i is the solution of the pressure, Q_i is the flow exiting from each outlet, and R_i, R and C are two resistors and a capacitance, respectively. To obtain the normal pulsatile pressure condition (shown in Fig. 3(a)), the values of these parameters were taken following the results obtained by Segers *et al.*[34] Then, Eq. (4) was solved using finite difference approximation of derivatives by the central difference method (Eq. (5)) in a code on RStudio, solving for p^{t+1}. Then, it was interpreted by the ANSYS Fluent software.

$$p^{t+1} = p^{t-1}\left(1 - \frac{2\Delta t}{RC}\right) + \frac{2\Delta t Q_i}{c}\left(1 + \frac{R_i}{R}\right) + 2\Delta t R_i \frac{dQ_i}{dt}. \tag{5}$$

In addition, we used Eq. (6) to relate the input flow and pressure difference (Hagen–Poiseuille equation.[35]).

$$dp = \frac{8\mu Q dl}{\pi r^4}. \tag{6}$$

By considering the axial differential equation, we obtain the expression shown in Eq. (7).

$$u = \varsigma \nabla p, \tag{7}$$

where $\varsigma = \frac{r^2}{8\mu}$.

With Eq. (7), we may derive different types of pressure differences if the inlet velocity (u) is known[21,36,37]; in fact, the inlet velocity is a boundary condition.

On the other hand, to study the relationship between the hemodynamic and geometric parameters, we used three cases of a high-pressure difference, three cases of a low-pressure difference and a base case of the pressure difference (Eq. (7)); therefore, we had seven cases altogether. For each case, we performed 60 simulations of the cerebral arteries (30 previously ruptured and 30 previously unruptured) whose setups are discussed in Sec. 2.3. Altogether, we carried out 420 simulations.

To obtain the low and high-pressure differences, we considered the results from the numerical studies of Torii *et al.*,[38] Cebral *et al.*[39] and Le,[40] that mentions some limits of the velocity inside the arteries in a physiological environment, being 0.45 and 1.45 times the normal pressure among branches, respectively. Hence, the inlet velocity condition (Eq. (7), normal hemodynamic state) was multiplied by 0.55, 0.70 and 0.85 (low-pressure differences) and 1.15, 1.30 and 1.45 (high-pressure differences). Also, we calculated the Windkessel pressure in all cases, being a maximum of 180 mmHg and a minimum of 70 mmHg.

2.3. *Numerical method and setup*

A mesh for each geometry must be considered to solve the transient Navier–Stokes equations by considering a non-Newtonian fluid. In our case, we used a mesh density of 1500 elements/mm^3 (shown in Fig. 4), in which we studied the difference between WSS (in the most influenced area of the aneurysm) at the systole time of the pulsatile blood flow with 250, 500, 1000, 2500, 3500 and 4500 elements/mm^3, respectively. The maximum difference is shown in Fig. 5, and it is below 2% between 1500 and 4500 elements/mm^3. The criteria values were selected for the time step and residual were 0.0001 s and 0.001, respectively.

The pressure implicit with splitting of operator (PISO) algorithm was used to solve the Navier–Stokes equations using the spatial discretization of the least squares cell based on the gradient, second-order pressure, and second-order upwind for the momentum. For the transient formulation, the second-order implicit method was used.

Finally, the Time-Averaged Wall Shear Stress (TAWSS $= \frac{1}{T}\int_0^T |\tau_w(\mathbf{x}, t)| dt$) on each cerebral aneurysm were computed by employing ANSYS, where this quantity was besides averaged over the area of each aneurysm during a cardiac cycle T. Consequently, TAWSS were related with the associated AR to obtain the corresponding relationships.

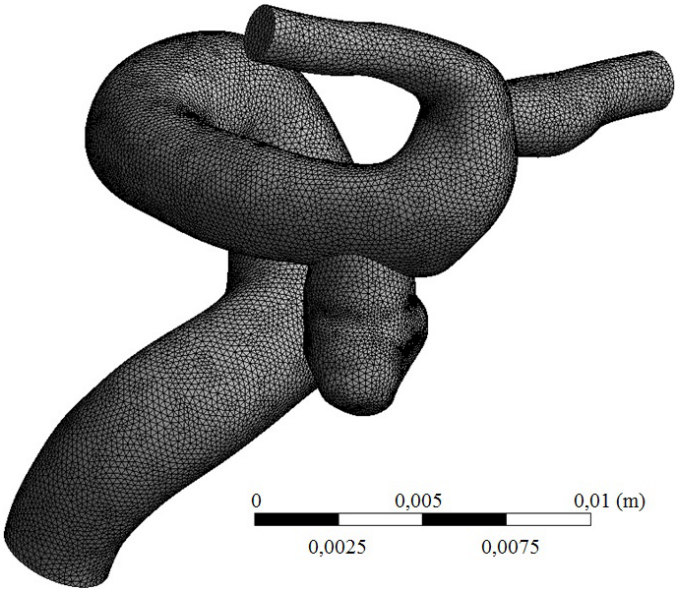

Fig. 4. Type of grid using 1500 elements/mm^3 for a case studied.

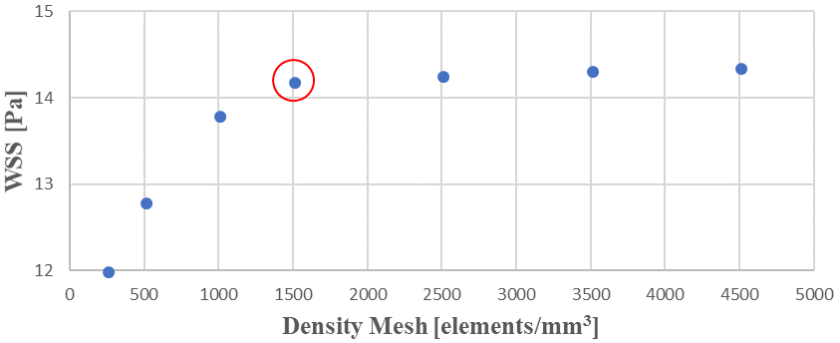

Fig. 5. Comparison of mesh results when WSS at systole time was calculated using different mesh densities. The difference of the computing time in ANSYS was almost 10 times between 4500 elements/mm^3 and 1500 elements/mm^3.

3. Results and Discussion

WSS on the wall of each cerebral aneurysm was computed in all the simulations (a case is shown in Fig. 6, where the maximum peaks represent the systolic time), then, we calculated TAWSS and the relationship between TAWSS and AR using an RStudio script code. It is important mentioning that WSS had a lower magnitude at the diastolic time than the systolic time, although the temporary form was maintained. For large aneurysms, we noticed that the maximum WSS was mainly

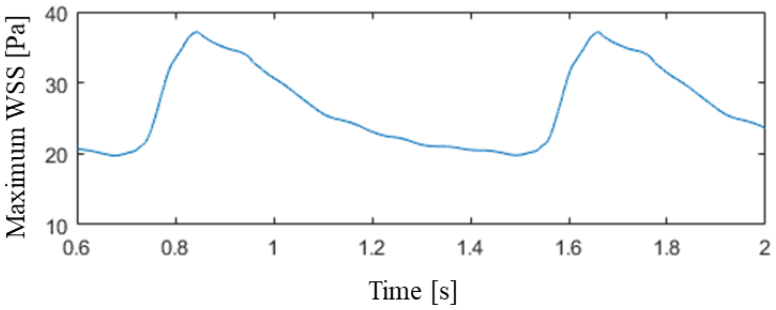

Fig. 6. Maximum WSS computed and located at the neck of an aneurysm for a normal pressure difference.

located at the neck of the aneurysms (shown in Figs. 7 and 8) due to the velocity vector inside of the cerebral artery was approximately 90° with respect to the wall of the aneurysm.[40] In addition, for large aneurysms, the flow enters the aneurysm generating vorticities without being significant at the dome.[41,42] On the other hand, when an aneurysm has a small size, the velocity streamlines are distributed throughout the surface area, and indeed, the rupture occurs at the dome.[43]

Out of 420 results, 12 of them are shown in Fig. 8, considering a normal pressure difference. With large aneurysms, maximum WSS was mainly located at the neck. On the other hand, with small aneurysms, maximum WSS is distributed throughout the surface area. Also, it is important to note that WSS is strongly correlated with the aneurysm rupture.[9,13]

A comparison of each slope of TAWSSs (vertical axis) variation with ARs (horizontal axis) are shown in Figs. 9 and 10 for previously unruptured and

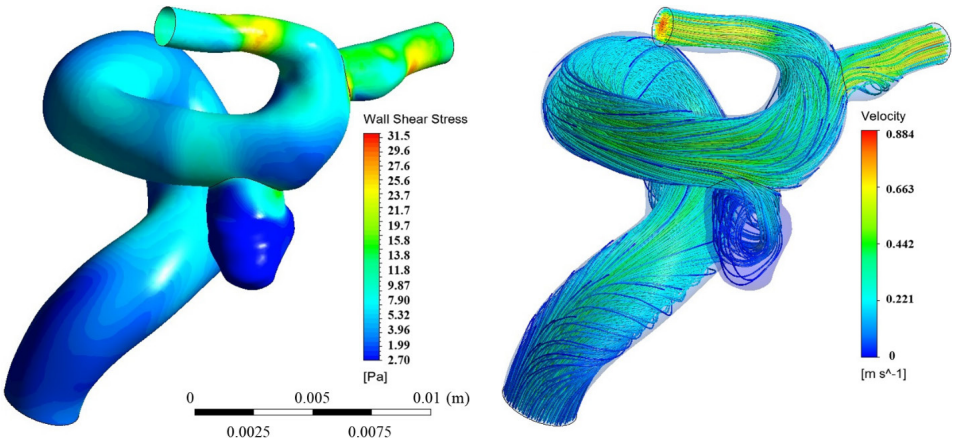

(a) (b)

Fig. 7. WSS (a) and velocity streamline (b) computed at a systolic time from ANSYS software. High WSS was localized at the neck of the aneurysm (AR = 2.88) where the flow was facing the wall.

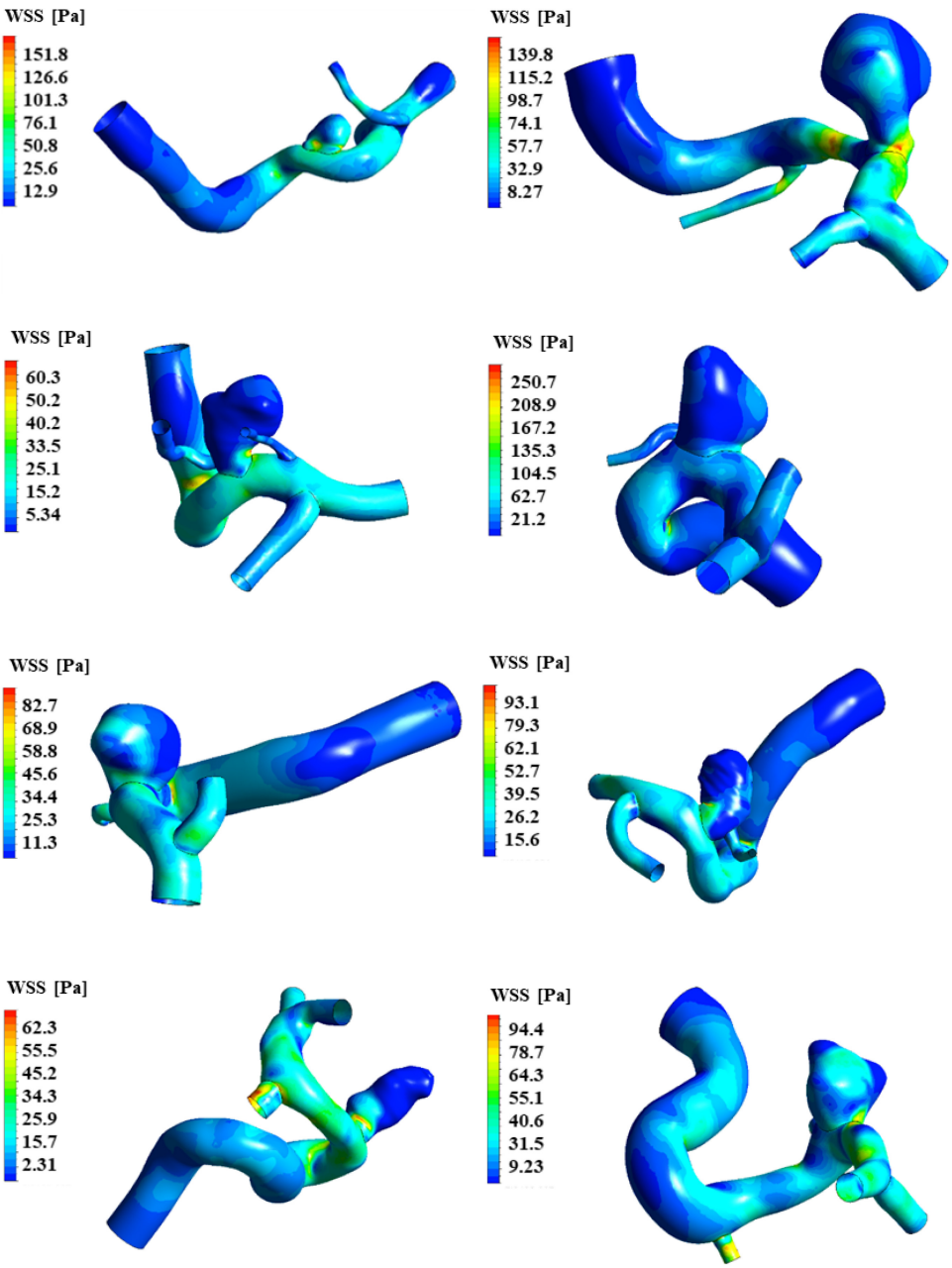

Fig. 8. Result of the WSS calculation at the systolic time in some random aneurysms selected for a normal pressure difference.

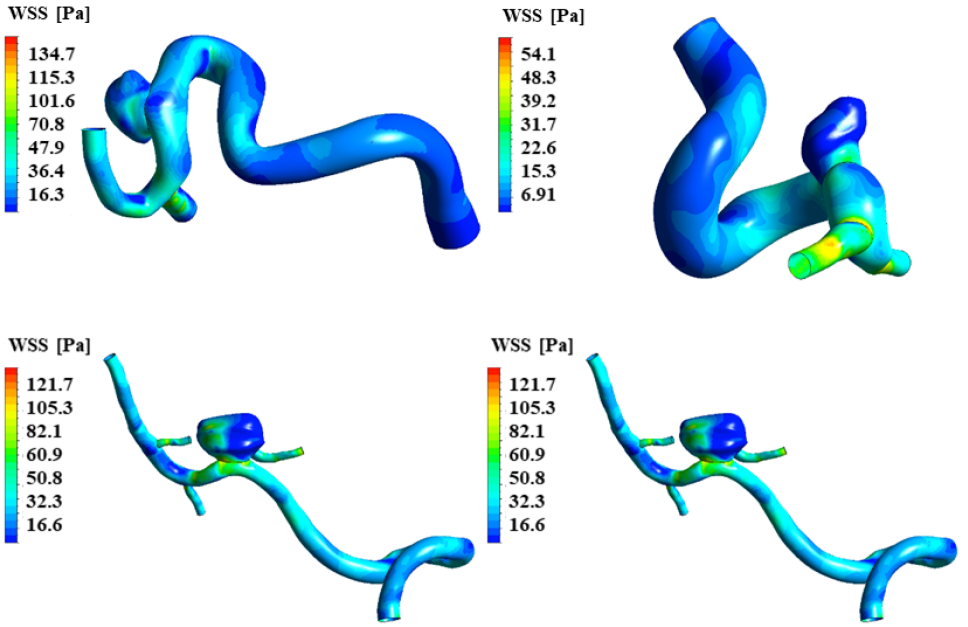

Fig. 8. (*Continued*)

previously ruptured aneurysms, respectively. We show the results of the seven cases of the pressure differences studied in this investigation, wherein each case had 30 different arteries that represent a variation of AR. We calculated the best fits to the distributions using a linear regression[44] on RStudio, where R^2 was greater than 88% for all values of TAWSS (statistic results are shown in Table 1). Standard deviation was homoscedastic in each case, standard errors were linear and P values were all lower than 0.0005. Consequently, the slopes fitted in the variation of TAWSS as a function of AR decreased linearly from the lowest to the largest pressure difference. Furthermore, the slopes of the previously unruptured aneurysms were smaller than the previously ruptured aneurysms. It oppositely occurs with the intercept in the vertical axis, being higher in the previously unruptured aneurysms, this is due to the ones that have a smaller surface area, and therefore, there is a greater distribution of velocity fields and WSSs than previously ruptured aneurysms.

On the other hand, measuring the condition of the pressure among branches and the AR in any patient, a slope may be associated, and then, a TAWSS may be estimated. It is important to consider that whether the value of TAWSS is low (high values of the ARs), then the aneurysm may be ruptured. Additionally, a study has shown that a low-WSS (high-AR) may have a significant role in the rupture of an aneurysm,[45] in accordance with our results.

Furthermore, we analyzed the relationship between TAWSS and other geometric parameters of the aneurysms, such as bottleneck and non-sphericity index

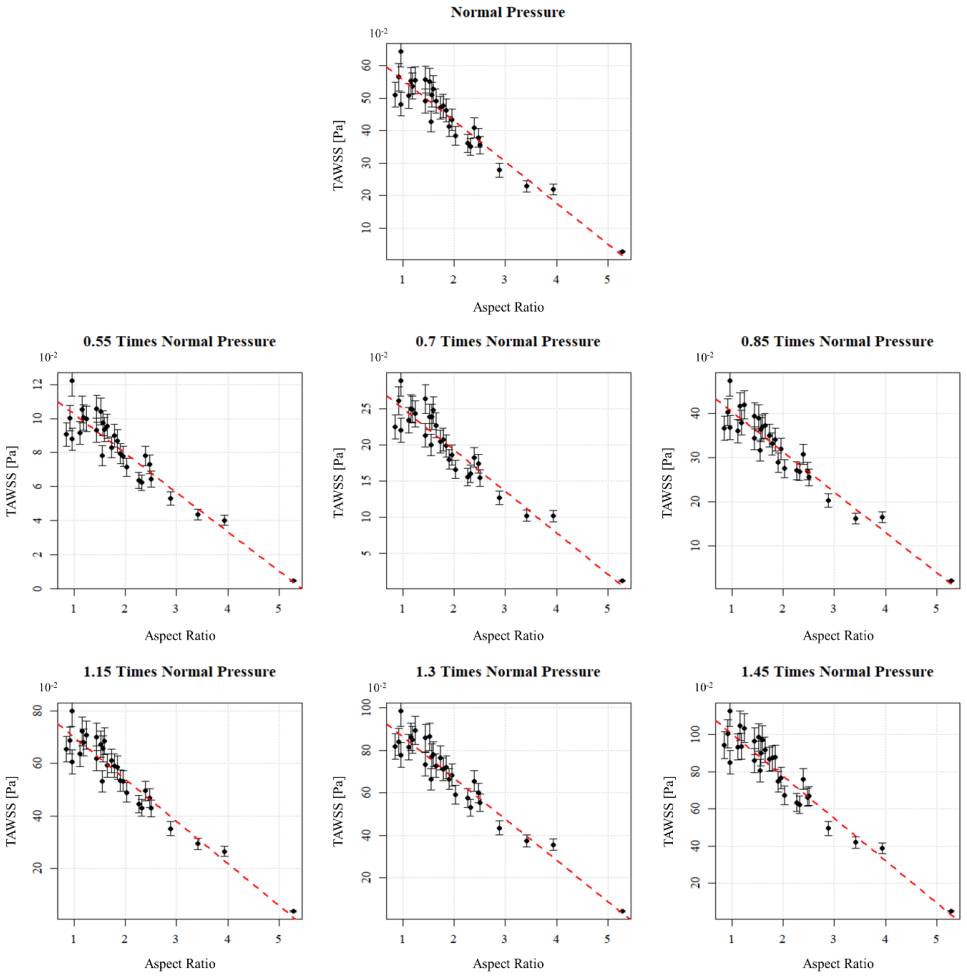

Fig. 9. Relationship of the previously unruptured aneurysm between the TAWSS and AR for the seven cases of the pressure difference conditions.

(these geometric parameters do not depend on the neck of the aneurysm); however, no relationships were found because TAWSS depends on the implicit velocity and is affected by the variations of the neck of the lateral saccular aneurysm.[40–42] For low values of the neck diameter (high values of the AR), TAWSS also has low values.

With respect to the limitations of this study, CFD techniques in cerebral aneurysms are a relatively new approach translating a well-established engineering technology into clinical research, being a real-world approximation.[46] Boundary conditions have an important role in any CFD problem, they are approximated by no-variation generalized waveforms, quantifying the hemodynamic differences between ruptured and unruptured aneurysms.[47] However, physiologic waveforms may also vary due to physical efforts or emotional excitement, resulting in a sudden

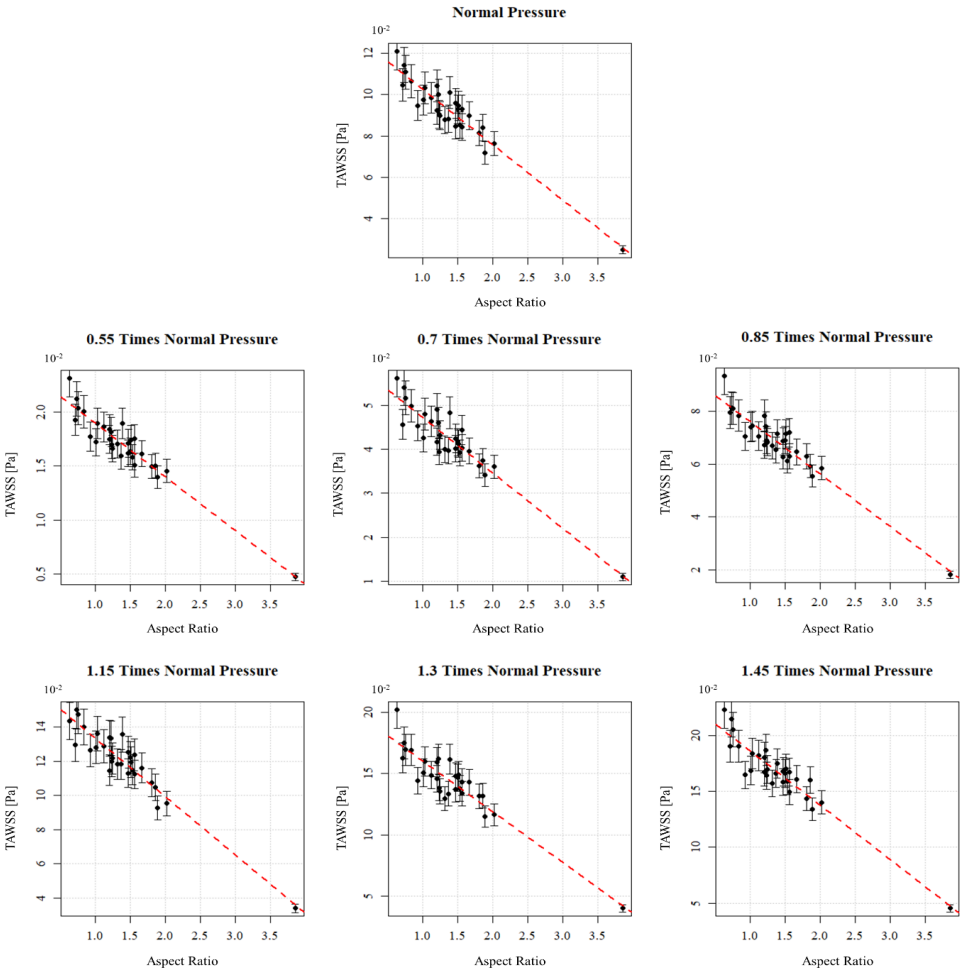

Fig. 10. Relationship of the previously ruptured aneurysm between the TAWSS and AR for the seven cases of the pressure difference conditions.

Table 1. Statistic values of the linear regression supervised-learning algorithm computed and summarized in each case in study.

Previously condition	Case	R^2	Slope ($\times 10^{-2}$)	Intercept ($\times 10^{-2}$)	Slope Std. error ($\times 10^{-2}$)	Intercept Std. error ($\times 10^{-2}$)
Unruptured	0.55 times	0.868	−2.31	12.59	0.167	0.359
	0.70 times	0.888	−5.72	30.72	0.376	0.809
	0.85 times	0.901	−9.12	49.54	0.561	1.208
	Normal	0.904	−12.58	68.09	0.762	1.639
	1.15 times	0.904	−15.98	85.84	0.964	2.07
	1.30 times	0.911	−19.37	105.75	1.125	2.42
	1.45 times	0.899	−22.72	123.16	1.417	3.03

Table 1. (*Continued*)

Previously condition	Case	R^2	Slope ($\times 10^{-2}$)	Intercept ($\times 10^{-2}$)	Slope Std. error ($\times 10^{-2}$)	Intercept Std. error ($\times 10^{-2}$)
Ruptured	0.55 times	0.900	−0.50	2.39	0.031	0.046
	0.70 times	0.871	−1.26	5.98	0.090	0.135
	0.85 times	0.897	−1.98	9.58	0.124	0.187
	Normal	0.898	−2.68	12.94	0.167	0.251
	1.15 times	0.893	−3.40	16.75	0.218	0.328
	1.30 times	0.881	−4.13	20.14	0.333	0.502
	1.45 times	0.883	−4.84	23.44	0.325	0.490

change in blood pressure and TAWSS. We propose to carry out another work that studies the relationship between TAWSS and AR considering the physiologic waveform variations and how close they are to the ideal model.

4. Conclusions

In this investigation, the effect of three low, normal and high-pressure differences among the branches of each artery on 60 human saccular cerebral aneurysm models were investigated using ANSYS simulations considering both the previously ruptured and unruptured aneurysms. In the result of each simulation for large aneurysms, we found that the maximum WSS was mainly located at the neck of the aneurysm due to the velocity vector that was normal with respect to the wall of the aneurysm, generating vorticities without being significant at the dome. On the other hand, TAWSS was related with respect to AR and a linear regression with negative slope was found for each case. Accordingly, while the pressure difference was higher, higher was the absolute value of the slope in each case. Also, the slope and intercept of the previously unruptured aneurysms was on average 4.7 times and 5.2 times the slope of the previously ruptured aneurysms, respectively. Greatest values of TAWSS in the unruptured previously aneurysms are due to the ones that have a smaller size, and therefore, these values have a greater distribution of the velocity fields and WSS on the walls.

Acknowledgment

Alfredo Aranda-Núñez would like to thank CONICyT/PCHA PhD fellowship No. 21140180.

References

1. Brisman J, Song J, Newell D, Cerebral aneurysms, *N Engl J Med* **355**:928–939, 2006.
2. Keedy A, An overview of intracranial aneurysms, *McGill J Med* **9**(2):141–146, 2006.
3. Pritz M, Cerebral aneurysm classification based on angioarchitecture, *J. Stroke Cerebrovasc Dis* **20**(2):162–167, 2011.

4. Wardalw J, White P, The detection and management of unruptured intracranial aneurysms, *Brain* **15**(5):1–12, 2000.
5. Phil W, Stehbens D, Etiology of intracranial berry aneurysms, *J Neurosurg* **70**(6):823–931, 1989.
6. Steiger H, Pathophysiology of development and rupture of cerebral aneurysms, *Neurochirurgica Suppl* **48**:1–57, 1990.
7. Xiang J, Natarajan S, Tremmel M, Ma D, Mocco J, Hopkins L, Siddiqui A, Levy E, Meng H, Hemodynamic-morphologic discriminants for intracranial aneurysm rupture, *Stroke*, **42**:144–152, 2010.
8. Cebral J, Mut F, Weir J, Putman C, Association of hemodynamic characteristics and cerebral aneurysm rupture, *Am J Neuroradiol* **32**:264–270, 2011.
9. Cebral J, Mut F, Weir J, Putman C, Quantitative characterization of the hemodynamic environment in ruptured and unruptured brain aneurysms, *Am J Neuroradiol* **32**:145–151, 2011.
10. Gibbons G, Dzau V, The emerging concept of vascular remodeling, *New Engl J Med* **330**(20):1431–1438, 1994.
11. Malek A, Seth A, Izumo S, Hemodynamic shear stress and its role in atherosclerosis, *Jama* **282**(2):2035–2042, 1999.
12. Shojima M, Oshima M, Tagaki K, Torii R, Hayakawa M, Katada K, Morita A, Kirino T, Magnitude and role of wall shear stress on cerebral aneurysm computational fluid dynamic study of 20 middle cerebral artery aneurysms, *J Am Heart Assoc* **35**(11):2500–2505, 2004.
13. Zang Z, Durka M, Kallmes D, Ding Y, Robertson A, Can aspect ratio be used to categorize intra-aneurysmal hemodynamics? A study of elastase induced aneurysms in rabbit, *J Biomech* **44**:2809–2816, 2011.
14. Evju O, Valen-Sendstad K, Mardal K, A study of wall shear stress in 12 aneurysms with respect to different viscosity models and flow conditions, *J Biomech* **46**(16):2802–2808, 2013.
15. Tateshima S, Chien A, Cebral J, Viñuela F, The effect of aneurysm geometry on the intra-aneurysmal flow condition, *Neuroradiology* **52**(12):1135–1141, 2010.
16. Ujiie H, Tamano Y, Sasaki K, Hori T, Is the aspect ratio a reliable index for predicting the rupture of a saccular aneurysm? *Neurosurg* **48**(3):495–503, 2001.
17. Hunter J, A method of raising the specific gravity of the blood, *J Physiol* **11**(1–2):115–120, 1890.
18. Hipple H, *Chemical Engineering for Non-Chemical Engineers*, ALChE, New Jersey, 2017.
19. Husain I, Labropulu F, Langdon C, Schwark J, A comparison of Newtonian and non-Newtonian models for pulsatile blood flow simulations, *J Mech Behav Mater* **21**(5–6):147–153, 2013.
20. Womersley J, Method for the calculation of velocity, rate of flow and viscous drag in arteries when the pressure difference is known, *J Physiol* **127**(3):553–563, 1955.
21. Zamir M, *The Physics of Pulsatile Flow*, Springer, New York, 2000.
22. Fluent A, ANSYS Workbench User's Guide, Ansys, Inc, Canonburg (2017).
23. Valencia A, Torres F, Effects of hypertension and pressure difference in a human cerebral aneurysm using fluid structure interaction simulations, *J Mech Med Biol* **17**(2):1–17, 2017.
24. Li S, Hoskins P, Anderson T, McDicken W, Measurement of mean velocity during pulsatile flow using time-avegared maximum frequency of doppler ultrasound waveforms, *Ultrasound Med Biol* **19**(2):105–113, 1993.
25. Blanco P, Volumetric blood flow measurement using Doppler ultrasound: Concerns about the technique, *J Ultrasound* **18**(2):201–204, 2015.

26. Baddeley A, Turner R, spatstat: An R package for analyzing spatial point patterns, *J Stat Softw* **12**(6):5–11, 2005.
27. DeWayne R, Derryberry R, *Fitting Fourier Series*, in Basic Data Analysis for Time Series with R, John Wiley & Sons, pp. 115–124, 2014.
28. Leopold P, Shandall A, Feustel P, Corson J, Shah D, Popp A, Fortune J, Leather R, Karmody A, Duplex scanning of the internal carotid artery: An assessment of cerebral blood flow, *Br J Surg* **74**(7):630–633, 1987.
29. Schoning M, Walter J, Scheel P, Estimation of cerebral blood flow through color duplex sonography of the carotid and vertebral arteries in healthy adults, *Stroke* **25**(1):17–22, 1994.
30. Scheel P, Ruge C, Schoning M, Flow velocity and flow volume measurements in the extracranial carotid and vertebral arteries in healthy adults: Reference data and the effects of age, *Ultrasound Med Biol* **26**(8):1261–1266, 2000.
31. Kamensky A, Dzenis Y, Mactaggart J, Desyatova A, Pipinos I, In vivo three-dimensional blood velocity profile shapes in the human common, internal, and external carotid arteries, *J Vasc Surg* **54**(4):1011–1020, 2011.
32. Ogedegbe G, Pickering T, Dphil M, Principles and techniques of blood pressure measurement, *Cardiol Clin* **28**(4):571–586, 2010.
33. Westerhof N, Bosman F, Vries C, Noordergraaf A, Analog studies of the human systemic arterial tree, *J Biomech* **2**(2):121–134, 1969.
34. Segers P, Rietzschel E, Buyzere MD, Stergiopulos N, Westerhof N, Bortel LV, Verdonck P, Gillebert T, Three-and-four-element Windkessel models: Assessment of their fitting performance in a large cohort of healthy middle-aged individuals, *J Eng Med* **222**(4):417–428, 2008.
35. Munson B, Young D, Okiishi T, Huebsch W, *Fundamentals of Fluid Mechanics*, John Wiley & Sons, New Jersey, 2009.
36. Wang L, Zhou Z, Shen M, Sun Y, Sun G, Hemodynamic numerical simulation and analysis of oscillatory blood flow in growing aneurysms, *Bio-Med Mater Eng* **24**(1):459–466, 2014.
37. Marzo A, Singh P, Reymond P, Stergiopulos N, Patel U, Hose R, Influence of inlet boundary conditions on the local haemodynamics of intracranial aneurysms, *Comput Methods Biomech Biomed Eng* **12**(4):431–444, 2008.
38. Torri R, Oshima M, Kobayashi T, Takagi K, Tezduyar T, Numerical investigation of the effect of hypertensive blood pressure on cerebral aneurysm-dependence of the effect on the aneurysm shape, *Int J Num Methods Fluids*, **54**(6–8):995–1009, 2007.
39. Cebral J, Mut F, Raschi M, Scrivano E, Ceratto R, Lylyk P, Putman C, Aneurysm rupture following treatment with flow-diverting stents: Computational hemodynamics analysis of treatment, *Am J Neuroradiol* **32**(1):27–33, 2011.
40. Le T, Borazjani I, Sotiropoulos F, Pulsatile flow effects on the hemodynamics of intracranial aneurysms, *J Biomech Eng* **132**(11):1–11, 2010.
41. Fisher C, Rossmann J, Effect of non-newtonian behavior on hemodynamics of cerebral aneurysms, *J Biomech Eng* **131**(9) 2009.
42. Pereira V, Brina O, Gonzalez A, Narata A, Bijilenga P, Schaller K, Lovlad K, Ouared R, Evaluation of the influence of inlet boundary conditions on computational fluid dynamics for intracranial aneurysms: A virtual experiment, *J Biomech* **46**(9):1531–1539, 2013.
43. Goubergrits L, Schaller J, Kertzscher U, Bruck NVD, Poethkow K, Petz C, Hege H, Spuler A, Statistical wall shear stress maps of ruptured and unruptured middle cerebral artery aneurysms, *J R Soc Interf* **9**(69):677–688, 2011.

44. Freedman D, *Statistical Models: Theory and Practice*, Cambridge University Press, Berkeley, 2009.
45. Qiu T, Jin G, Xing H, Lu H, Association between hemodynamics, morphology, and rupture risk of intracranial aneurysms: A computational fluid modeling study, *Neurol Sci* **38**(6):1009–1018, 2017.
46. Karmonik C, Toward improving fidelity of computational fluid dynamics simulations: Boundary conditions matter, *Am J Neuroradiol* **35**(8):1549–1550, 2014.
47. Byrne G, Mut F, Cebral J, Quantifying the large-scale hemodynamics of intracranial aneurysms, Association of hemodynamic characteristics and cerebral aneurysm rupture, Wall shear stress on ruptured and unruptured intracranial aneurysms at the internal carotid artery, *Am J Neuroradiol* **35**(2):333–338, 2014.